Optics Letters

Controllable photonic crystal with periodic Raman gain in a coherent atomic medium

Zhaoyang Zhang,[1,2] Jingliang Feng,[1] Xing Liu,[2] Jiteng Sheng,[3] Yiqi Zhang,[2] Yanpeng Zhang,[2,5] and Min Xiao[1,4,*]

[1]Department of Physics, University of Arkansas, Fayetteville, Arkansas 72701, USA
[2]Key Laboratory for Physical Electronics and Devices of the Ministry of Education & Shaanxi Key Laboratory of Information Photonic Technique, Xi'an Jiaotong University, Xi'an 710049, China
[3]State Key Laboratory of Precision Spectroscopy, East China Normal University, Shanghai 200062, China
[4]National Laboratory of Solid State Microstructures and School of Physics, Nanjing University, Nanjing 210093, China
[5]e-mail: ypzhang@mail.xjtu.edu.cn
*Corresponding author: mxiao@uark.edu

Received 27 December 2017; revised 18 January 2018; accepted 18 January 2018; posted 19 January 2018 (Doc. ID 318502); published 14 February 2018

With two sets of standing-wave fields built in a thermal rubidium vapor cell, we have established a controllable photonic crystal with periodic gain in a coherently prepared *N*-type four-level atomic configuration. First, the photonic lattice constructed by a resonant standing-wave coupling field results in a spatially modulated susceptibility and makes the signal field diffract in a discrete manner under the condition of electromagnetically induced transparency. Then, with the addition of the standing-wave pump field, the *N*-type atomic medium can induce a periodic Raman gain on the signal field, which can be effectively controlled by tuning the pertinent atomic parameters. The experimental demonstration of such a real-time reconfigurable photonic crystal structure with periodic Raman gain can pave the way for realizing desired applications predicted in the gain-modulated periodic optical systems. © 2018 Optical Society of America

OCIS codes: (020.1335) Atom optics; (050.5298) Photonic crystals; (020.1670) Coherent optical effects.

https://doi.org/10.1364/OL.43.000919

The light propagation dynamic behaviors in artificial optical lattices have caught the interest of the scientific community over a long time, including nonlinear optics [1], Bose–Einstein condensates [2], basic quantum mechanical effects [3,4], and, recently, non-Hermitian optics [5]. Generally, such discrete periodic arrays are formed by coupled optical waveguides with equal spatial distance and can provide an effective platform to demonstrate a range of unattainable properties in homogeneous bulk media. The flow of light through such a kind of periodic environment is mainly manipulated by spatially engineering the refractive index (experienced by the incident light) in a periodic manner [6,7]. Under this mechanism, many interesting effects with fundamental importance for optical information science have been demonstrated, such as discrete diffractions [8], optical solitons [9], optical Bloch oscillation and Zener tunneling [10], and optical analogs of quantum random walks [11].

Furthermore, by introducing periodic gain into such photonic crystal structures, they can provide new routes to explore and improve the related applications covering self-collimation/diffraction-free propagation [12], spatial frequency filtering [13], shaping of light pulses [14], and properties in parity-time symmetry [15,16]. So far, most of the studies involving gain-modulated lattices are theoretical due to various difficulties, for example, the restriction on the connection between the real and imaginary parts of the refractive index as imposed by Kramers–Kronig relations [17], in experimentally generating spatially extended periodic gain structures. Fortunately, light-induced atomic coherence in multi-level atomic configurations can provide an effective solution for engineering desired refractive index profiles [18,19]. Particularly, electromagnetically induced transparency (EIT) [20,21] and induced Raman gain can be used to easily construct controllable gain/absorption and nonlinear properties [22] in multi-level atoms. The required Raman gain comes from a light amplification and can be created in an EIT window under the condition without (corresponding to normal dispersion) or with (anomalous dispersion) population inversion driven by a weak or strong pump field, respectively [23]. For instance, the optical waveguiding effect [8], electromagnetically induced Talbot effect [24], photonic band gap [25], and parity-time symmetric optical lattices [5] have already been effectively realized by spatially modulating the refractive index under the EIT regime in multi-level atomic configurations. Also, coherent Raman processes can provide a powerful solution for investigating many interesting effects, such as quantum memories [26,27].

In this Letter, we experimentally construct a Raman-gain-modulated photonic crystal structure with the assistance of two standing-wave laser fields in a four-level atomic assembly by spatially engineering the refractive index. The *N*-type

four-level atomic medium is driven by a signal field, a coupling field, and a pump field. The standing-wave coupling field propagating along the z direction can induce the lattice in the transverse direction x. With the weak Gaussian signal field injected into the induced optical lattice, a discrete diffraction pattern is observed under the EIT condition. Then, the addition of a standing-wave pump field can lead to periodic Raman gain [23] on the signal field. The observed gain can be effectively manipulated and optimized by controlling the parameters, such as the atomic density and the frequency detunings and intensities of laser fields.

Figure 1(a) shows the sketch for the experiment. Three laser fields are incident into a vapor cell filled with ^{85}Rb atoms to couple with an N-type four-level atomic structure, consisting of two ground levels $5^2S_{1/2}$, $F = 2(|1\rangle)$, and $F = 3(|2\rangle)$ and two excited levels $5^2P_{1/2}(|3\rangle)$ and $5^2P_{3/2}(|4\rangle)$, as depicted in Fig. 1(b). Transition $|2\rangle \rightarrow |3\rangle$ is driven by the standing-wave coupling field, which is formed by two elliptically shaped beams $\boldsymbol{E}_c$ and $\boldsymbol{E}_c'$ (wavelength $\lambda_c = 795.0$ nm, frequency ω_c) from the same external cavity diode laser (ECDL2). The two co-propagating coupling beams with the same angle of $\theta = 0.2°$ on both sides of the z axis intersect at the center of the atomic vapor cell, and the space between the interference fringes is $d_c = \lambda_c/(2 \times \sin\theta) \approx 114$ μm. When the Gaussian signal field $\boldsymbol{E}_s$ ($\lambda_s = 795.0$ nm, frequency ω_s) connecting the transition $|1\rangle \rightarrow |3\rangle$ passes through such a coupling lattice along the z direction, a discrete diffraction pattern can be observed [recorded by a charge coupled device (CCD) camera)] at the output surface of the cell by properly setting the temperature of the medium, intensities and frequencies of corresponding laser beams, and the periodicity of the induced lattices. After two pump laser beams $\boldsymbol{E}_p$ and $\boldsymbol{E}_p'$ ($\lambda_p = 780.2$ nm, ω_p) from the same ECDL3, partially overlapped with $\boldsymbol{E}_c$ and $\boldsymbol{E}_c'$, respectively, are injected into the vapor cell to establish the pump-field lattice (overlapping with the coupling lattice) to excite the transition $|1\rangle \rightarrow |4\rangle$, the diffracted signal field can experience a Raman gain on its bright fringes due to the four-level N-type configuration [23]. The angles for generating the two standing-wave fields are not strictly the same due to the different wavelengths of the coupling and pump fields. To monitor the frequency detunings of the three laser fields, we inject three beams $\boldsymbol{E}_s''$, $\boldsymbol{E}_c''$, and $\boldsymbol{E}_p''$ (from the same ECDLs as $\boldsymbol{E}_s$, $\boldsymbol{E}_c'$, and $\boldsymbol{E}_p'$, respectively) into another auxiliary Rb cell [as shown in the dashed box in Fig. 1(a)] to establish the same four-level system and observe the output spectrum of $\boldsymbol{E}_S$ in the frequency domain. Here, the frequency detunings for the signal, coupling, and pump fields are defined as $\Delta_s = \omega_{31} - \omega_s$, $\Delta_c = \omega_{32} - \omega_c$, and $\Delta_p = \omega_{41} - \omega_p$, respectively. Figure 1(c) shows the transmission spectra of $\boldsymbol{E}_S$ under different beam arrangements with the lower, middle, and upper curves representing the absorption (corresponding to the transition $|1\rangle \rightarrow |3\rangle$), EIT window ($|1\rangle \rightarrow |2\rangle \rightarrow |3\rangle$) and Raman gain ($N$-type four-level configuration), respectively. To achieve the EIT condition with high efficiency in the current three-level Λ-type system, the signal and coupling lasers should be weak ($\Omega_s < 10$ MHz) and strong ($\Omega_s \approx 100$ MHz), respectively. Here, Ω_f ($f = s, c$ and p) is the Rabi frequency of field $\boldsymbol{E}_f$. Also, the two fields co-propagate along the same direction to overcome the Doppler effect in thermal atoms.

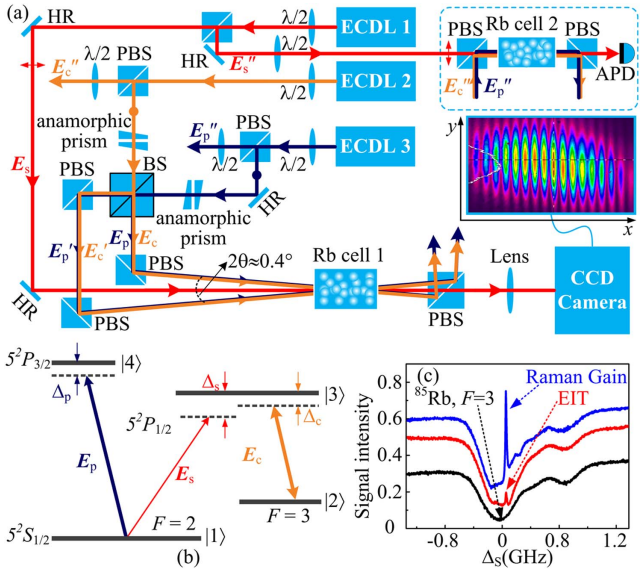

Fig. 1. (a) Experimental setup. The setup in the dashed box is for generating the EIT and Raman gain spectra (detected by the APD) to calibrate the detunings of lasers. ECDL, external cavity diode laser; $\lambda/2$, half-wave plate; HR, high-reflectivity mirror; PBS, polarization beam splitter; BS, beam splitter; APD, avalanche photodetector; CCD, charge coupled device. (b) N-type energy-level configuration. (c) Raman gain (upper blue curve) and EIT (middle red curve) spectra (with the same widths of about 30 MHz) versus the detuning of the signal field. The lower black curve represents the absorption of the signal field corresponding to the transition ^{85}Rb, $F = 3 \rightarrow F'$.

The optical response of the signal field can be described by the susceptibility χ, which is proportional to the atomic density N and the density-matrix element ρ_{31} for the transition $|1\rangle \leftrightarrow |3\rangle$. ρ_{31} can be obtained via the density-matrix equations and controlled via the parameters, such as field intensities and frequency detunings [28]. Considering $n = \sqrt{1+\chi} \approx 1 + \chi/2$, $\chi = \chi' + \chi''$, and $n = n_0 + n_R + in_I$ (n is the refractive index, and $n_0 = 1$ is the background index of the medium), the real and imaginary components of the refractive index can be written as $n_R \approx \chi'/2$, and $n_I \approx \chi''/2$, respectively. With the coupling intensity spatially modulated, n_R (representing dispersion) and n_I (absorption) for $\boldsymbol{E}_s$ can behave as a periodic function of the transverse coordinate x under the EIT condition [5,8]. By introducing the intensity-modulated pump field, the imaginary n_I can become alternately above and below zero along x [28]. When the imaginary n_I is negative (positive), the signal field experiences gain (absorption/loss).

Figure 2 shows the observed transmission images of the signal field under various conditions. First, with the frequency detuning set to be far away from its single-photon resonant point $\Delta_s = 0$, the signal field does not interact with the atoms and experiences no gain or loss, as shown in Fig. 2(a). The white solid curves (from the CCD camera) at the bottom and left side of each picture represent the intensity profiles of the detected image. A dashed curve copied from the profile in Fig. 2(a) is added, as a reference, in each subsequent figure to indicate the original intensity of the signal field. With the detuning set at $\Delta_s = 100$ MHz relative to the $5S_{1/2}$, $F = 3 \rightarrow 5P_{1/2}$, $F' = 3$ transition of ^{85}Rb, the Gaussian beam is greatly absorbed, as given in Fig. 2(b). When the signal field propagates through the pump lattice, it shows very fuzzy stripes

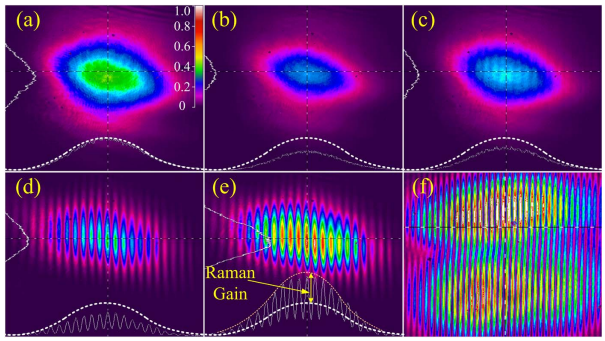

Fig. 2. Detected signal field under different conditions. (a) The signal field is detuned by $\Delta_s = -700$ MHz from the resonance. A dashed curve is added to copy the white solid curve, which represents the intensity profile of the image. The unit of the color bar is milliwatts (mW). (b) The signal field only at detuning $\Delta_s = 100$ MHz experiences large absorption. (c) With the signal field and standing-wave pump field turned on. Due to the rather demanding conditions for EIT in this V-type configuration, the output signal field does not experience a clear diffraction. (d) With the signal field and standing-wave coupling field turned on to satisfy the EIT condition. (e) The observed periodic Raman gain with all three fields on. (f) The observed interference fringes of the coupling (upper) and pump (lower) beams at their intersection.

[Fig. 2(c)] due to the rather demanding conditions for realizing EIT in a V-type configuration ($|1\rangle \rightarrow |3\rangle \rightarrow |4\rangle$) [29]. Although no EIT window is induced, the output image in Fig. 2(c) is still stronger than the purely absorbed image in Fig. 2(b). This enhancement is caused by the optical pumping (OP) effect, which can reduce the absorption of the signal field similar to the EIT effect [30]. Then, with the pump beams off and coupling beams on, the coupling lattice discretizes the Gaussian signal beam into a stripe pattern [Fig. 2(d)], which indicates that $\boldsymbol{E}_s$ feels a periodically modified refractive index [8]. Such discrete diffraction can clearly occur in a frequency range of ± 20 MHz near the two-photon resonant point $\Delta_s - \Delta_c = 0$. The introduction of the periodic pump field can induce Raman gain on the signal field [23] and establish a gain array. By comparing the output signal image in Fig. 2(e) with its original intensity profile [the added dashed curve in Fig. 2(a)], one can clearly see the generated periodic gain (above the dashed curve) and loss (below the dashed curve) values. Figure 2(f) demonstrates the two formed standing-wave fields observed at the central position of the atomic cell. Here, in order to show the two periodic fields more clearly, we separate the two interference fringes along the y direction. During the experiment, the two standing waves are almost perfectly overlapped inside the medium.

Figure 3 reveals the dependence of the induced periodic Raman gain on the total power P of the two pump beams. For the case in Fig. 3(a) with the pump field turned off ($P = 0$), the signal field exhibits the simple discrete diffraction under EIT. With the pump field on and its total intensity being weak ($P = 5$ mW), the absorption is still dominant. The EIT due to the coupling field and OP effect from the pump field can both reduce the near-resonant absorption of the signal field, so the observed image in Fig. 3(b) is stronger than the pure EIT case shown in Fig. 3(a). With the P increased to 10 mW, the spatially extended Raman gain can be clearly seen.

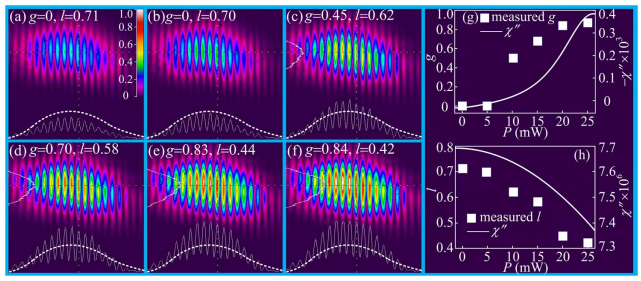

Fig. 3. Evolution of the periodic Raman gain by increasing the intensity of the pump field. The unit of the color bar is mW. The dashed curve is the same as the one in Fig. 2(a). The total power P of the two pump beams are (a) 0, (b) 5 mW, (c) 10 mW, (d) 15 mW, (e) 20 mW, and (f) 25 mW, respectively. g and l are the coefficients for Raman gain and loss, respectively. (g) and (h) The dependences of g and l on the pump power, respectively. The squares are experimental observations, and the solid curves are the theoretical susceptibility according to Ref. [28]. The theoretical parameters for (g) are $\Omega_s \approx 66$ MHz, $\Omega_c = 2.2 \times 2\pi$ MHz, $\Delta_s = -15.16 \times 2\pi$ MHz, $\Delta_c = -85.62$ MHz, $\Delta_p = 34.1$ MHz, and Ω_p growing from 0 to 64 MHz. The conditions for (h) are the same as (g) except for $\Omega_c = 2\pi$ MHz and Ω_p increasing from 0 to 3 MHz.

Furthermore, the Raman gain can continually grow with the power P adjusted from 10 mW to 20 mW. However, the gain under $P = 25$ mW shows little change compared to that under $P = 20$ mW. This tendency is basically consistent with the theoretical curve for the same four-level atomic configuration [23], which predicted that the Raman gain first grows with the pump intensity, then reaches a saturation, and finally decreases with further increased pump intensity. Due to the limitation of the output power of ECDL3, the decrease of the Raman gain under the condition of very large P is not observed. Meanwhile, one can see that the absorption/loss experienced by the dark fringes of the signal field can be better suppressed at the larger pump power, which leads to a stronger OP effect. Figures 3(g) and 3(h) are the dependences for the respective gain and loss coefficients on the pump power. The gain (loss) coefficient $g(l)$ is given as the ratio between the intensity of Raman gain (absorption) and the intensity of the incident signal field.

Figure 4 demonstrates the dependence of Raman gain on the temperature T of the medium. When T gradually

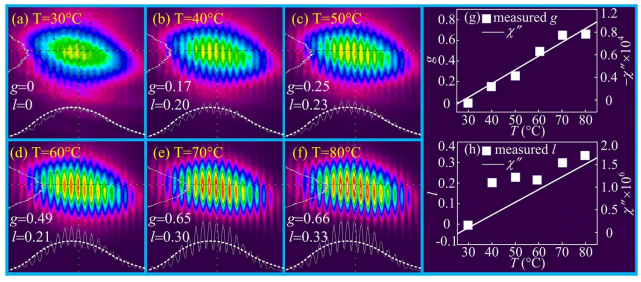

Fig. 4. Evolution of the Raman gain by increasing the temperature of the medium from 30°C to 80°C. The dashed curve on the bottom of each figure is the same as that in Fig. 2(a). Each figure shares the same color bar as Fig. 3. (g) and (h) The dependency curves of gain (g) and loss (l) coefficients on the temperature, respectively. The squares are experimental observations, and the solid curve is the calculated susceptibility with the same parameters as Fig. 3.

varies from the room temperature (30°C, atomic density $\sim 2.3 * 10^{10}$ cm^{-3}) to 80°C (atomic density $\sim 2.8 * 10^{12}$ cm^{-3}), then the Raman gain becomes even more obvious. This can be easily understood since the imaginary part (gain/absorption) of the refractive index is proportional to the atomic density [28]. However, compared to the observation in Fig. 4(e) at $T = 70$°C, the gain at 80°C experiences only a little change. This demonstrates the competition between the generation and propagation of the gain inside the medium [31]. For a lower temperature, the gain increases with the atomic thermal motion, while its loss during the propagation is weak. For a higher temperature, the loss inside the cell is greatly enhanced, and the observed gain out of the cell increases much slower. In principle, the absorption (described by n_I) at the dark fringes on the signal field can also increase with the temperature, similar to the gain. However, due to the increased OP effect at a higher temperature, the absorption is effectively suppressed. The intensities at the dark fringes remain almost unchanged at different temperatures, which indicate that the enhancement due to OP and the absorption have reached a balance. According to the experimental observations, the dependency curves for the gain and loss coefficients on the temperature are given in Figs. 4(g) and 4(h), respectively.

In summary, by making use of the modified optical properties, including absorption and dispersion caused by EIT and Raman gain in an N-type four-level atomic configuration, we have experimentally realized a multi-parameter tunable gain array by launching a Gaussian signal beam into two sets of optically induced one-dimensional optical lattices. Such a gain-modulated photonic crystal structure can be easily reconfigurable in real-time by changing the temperature of the medium, the distance between the fringes of the standing wave, and the parameters of the laser fields. Furthermore, owing to the greatly enhanced nonlinear properties, such a photonic crystal structure in a coherently prepared atomic system provides a unique platform to investigate intriguing nonlinear/quantum light dynamical characteristics predicted in multi-channel lattice potentials for the refractive index and can serve as a new route for exploring useful applications in coherent optical information processing.

Funding. National Key R&D Program of China (2017YFA0303703); National Natural Science Foundation of China (NSFC) (61605154); Natural Science Foundation of Shaanxi Province (2017JQ6039); China Postdoctoral Science Foundation (2016M600776, 2017T100734); Postdoctoral Science Foundation of Shaanxi Province (2017BSHYDZZ54).

REFERENCES

1. G. Bartal, O. Cohen, H. Buljan, J. W. Fleischer, O. Manela, and M. Segev, Phys. Rev. Lett. **94**, 163902 (2005).
2. O. Morsch and M. Oberthaler, Rev. Mod. Phys. **78**, 179 (2006).
3. I. Foulger, S. Gnutzmann, and G. Tanner, Phys. Rev. Lett. **112**, 070504 (2014).
4. A. Eckardt, Rev. Mod. Phys. **89**, 011004 (2017).
5. Z. Zhang, Y. Zhang, J. Sheng, L. Yang, M.-A. Miri, D. N. Christodoulides, B. He, Y. Zhang, and M. Xiao, Phys. Rev. Lett. **117**, 123601 (2016).
6. I. L. Garanovich, S. Longhi, A. A. Sukhorukov, and Y. S. Kivshar, Phys. Rep. **518**, 1 (2012).
7. D. N. Christodoulides, F. Lederer, and Y. Silberberg, Nature **424**, 817 (2003).
8. J. Sheng, J. Wang, M.-A. Miri, D. N. Christodoulides, and M. Xiao, Opt. Express **23**, 19777 (2015).
9. J. W. Fleischer, T. Carmon, M. Segev, N. K. Efremidis, and D. N. Christodoulides, Phys. Rev. Lett. **90**, 023902 (2003).
10. Y. Zhang, D. Zhang, Z. Zhang, C. Li, Y. Zhang, F. Li, M. R. Belić, and M. Xiao, Optica **4**, 571 (2017).
11. A. Peruzzo, M. Lobino, J. C. F. Matthews, N. Mastsuda, A. Politi, K. Poulios, X. Zhou, Y. Lahini, N. Ismail, K. Worhoff, Y. Bromberg, Y. Silberberg, M. G. Thompson, and J. L. Obrien, Science **329**, 1500 (2010).
12. K. Staliunas, R. Herrero, and R. Vilaseca, Phys. Rev. A **80**, 013821 (2009).
13. L. Maigyte and K. Staliunas, Appl. Phys. Rev. **2**, 011102 (2015).
14. Y. Loiko, M. Botey, R. Herrero, and K. Staliunas, Opt. Express **20**, 11271 (2012).
15. Z. Lin, H. Ramezani, T. Eichelkraut, T. Kottos, H. Cao, and D. N. Christodoulides, Phys. Rev. Lett. **106**, 213901 (2011).
16. K. G. Makris, R. El-Ganainy, D. N. Christodoulides, and Z. H. Musslimani, Phys. Rev. Lett. **100**, 103904 (2008).
17. S. A. R. Horsley, M. Artoni, and G. C. La Rocca, Nat. Photonics **9**, 436 (2015).
18. M. O. Scully, Phys. Rev. Lett. **67**, 1855 (1991).
19. L. Pei, X. Lu, J. Bai, X. Miao, R. Wang, L. Wu, S. Ren, Z. Jiao, H. Zhu, P. Fu, and Z. Zuo, Phys. Rev. A **87**, 063822 (2013).
20. S. E. Harris, Phys. Today **50**(7), 36 (1997).
21. J. Gea-Banacloche, Y. Li, S. Jin, and M. Xiao, Phys. Rev. A **51**, 576 (1995).
22. M. Xiao, Y. Li, S. Jin, and J. Geabanacloche, Phys. Rev. Lett. **74**, 666 (1995).
23. H. Kang, L. Wen, and Y. Zhu, Phys. Rev. A **68**, 063806 (2003).
24. Z. Zhang, X. Liu, D. Zhang, J. Sheng, Y. Zhang, Y. Zhang, and M. Xiao, Phys. Rev. A **97**, 013603 (2018).
25. Z. Zhang, D. Ma, Y. Zhang, M. Cao, Z. Xu, and Y. Zhang, Opt. Lett. **42**, 1059 (2017).
26. M. Dąbrowski, R. Chrapkiewicz, and W. Wasilewski, Opt. Express **22**, 26076 (2014).
27. N. Prajapati, G. Romanov, and I. Novikova, J. Opt. Soc. Am. B **34**, 1994 (2017).
28. J. Sheng, M. A. Miri, D. N. Christodoulides, and M. Xiao, Phys. Rev. A **88**, 041803 (2013).
29. Y. Wu and X. Yang, Phys. Rev. A **71**, 053806 (2005).
30. Z. Zhang, X. Xue, C. Li, S. Cheng, L. Han, H. Chen, H. Zheng, and Y. Zhang, Opt. Commun. **285**, 3627 (2012).
31. Z. Zhang, F. Wen, J. Che, D. Zhang, C. Li, Y. Zhang, and M. Xiao, Sci. Rep. **5**, 15058 (2015).